Journal of
*Composites Science*

MDPI

*Article*

# Mechanical Properties and Thermal Conductivity of Y-Si and Gd-Si Silicides: First-Principles Calculations

**Kexue Peng [1,2], Panxin Huang [1], Guifang Han [1,*], Huan Liu [1], Weibin Zhang [1], Weili Wang [1] and Jingde Zhang [1]**

[1] Key Laboratory for Liquid-Solid Structural Evolution and Processing of Materials (Ministry of Education), School of Materials Science and Engineering, Shandong University, Jinan 250061, China
[2] Xinjiang Key Laboratory of High Value Green Utilization of Low-Rank Coal, School of Physics and Materials Science, Changji University, Changji 831100, China
* Correspondence: gfhan@sdu.edu.cn

**Abstract:** The traditional Si bonding layer in environmental barrier coatings has a low melting point (1414 °C), which is a significant challenge in meeting the requirements of the next generation higher thrust-to-weight ratio aero-engines. To seek new bonding layer materials with higher melting points, the mechanical properties of Y-Si and Gd-Si silicides were calculated by the first-principles method. Subsequently, empirical formulae were employed to compute the sound velocities, Debye temperatures, and the minimum coefficients of thermal conductivity for the YSi, $Y_5Si_4$, $Y_5Si_3$, GdSi, and $Gd_5Si_4$. The results showed that $Y_5Si_4$ has the best plasticity and ductility among all these materials. In addition, $Gd_5Si_4$ has the minimum Debye temperature (267 K) and thermal conductivity (0.43 W $m^{-1}$ $K^{-1}$) compared with others. The theoretical calculation results indicate that some silicides in the Y-Si and Gd-Si systems possess potential application value in high-temperature bonding layers for thermal and/or environmental barrier coating.

**Keywords:** first-principles calculations; Y-Si system; Gd-Si system; mechanical properties; thermal conductivity



**Citation:** Peng, K.; Huang, P.; Han, G.; Liu, H.; Zhang, W.; Wang, W.; Zhang, J. Mechanical Properties and Thermal Conductivity of Y-Si and Gd-Si Silicides: First-Principles Calculations. *J. Compos. Sci.* **2024**, *8*, 221. https://doi.org/10.3390/jcs8060221

Academic Editor: Stelios K. Georgantzinos

Received: 1 May 2024
Revised: 22 May 2024
Accepted: 7 June 2024
Published: 12 June 2024



## 1. Introduction

The melting point of the traditional Si bond layer, which is 1414 °C, limits its application temperature in environmental barrier coatings (EBCs) [1]. Furthermore, the oxidation product, $SiO_2$, undergoes phase transformations accompanied by volume changes (~4.3%), which tends to cause the coating to crack [2,3]. Considering that the coefficient of thermal expansion (CTE) of $HfSiO_4$ (3.6–6.6 × $10^{-6}$ °$C^{-1}$ [4]) matches well with that of the SiC matrix (4.5 × $10^{-6}$ °$C^{-1}$ [5]), and given its good phase stability, $HfO_2$ was incorporated into the Si bond layer to dynamically convert $SiO_2$ into $HfSiO_4$ phase [6,7]. However, $HfO_2$ has a much higher oxygen diffusion rate, which accelerates the oxidation of the Si bond layer [8]. Although the oxidation resistance and the service life were improved by optimizing the content and distribution of $HfO_2$ [9,10], the service temperature did not improve, posing a challenge in fulfilling the demands for the next generation aero-engines with a higher thrust-to-weight ratio.

$Y_2SiO_5$ exhibits minimal oxygen permeability across a broad temperature spectrum, reaching a permeability of $10^{-10}$ kg/(m·s) at 1973 K [11]. Additionally, it demonstrates a CTE of 5–8 × $10^{-6}$ °$C^{-1}$, while $Y_2Si_2O_7$ has a CTE of 3.90 × $10^{-6}$ °$C^{-1}$ [11], which matches well with the SiC matrix when used in combination [12]. Yttrium silicides ($Y_xSi_y$) have much higher melting points than that of Si. And their oxidation products, $Y_2O_3$ and $SiO_2$, will react with each other to form $Y_2SiO_5$ and/or $Y_2Si_2O_7$, which have good environmental barrier properties. This strategy simultaneously increases not only the operating temperature of the bond layer but also its service life. The same applies to the rare earth silicate $Gd_2SiO_5$, which has a relatively low thermal conductivity and excellent corrosion resistance [13,14], and has been extensively studied as a coating material in recent

years [15,16]. Some gadolinium silicides ($Gd_xSi_y$) also have high melting points and good phase structural stability, making them promising candidates for use as high-temperature bonding layer materials.

When a certain material is used as a bond layer, it is important to consider not only its temperature resistance and oxidation resistance, but also its mechanical properties and thermal conductivity. The coating material should have good ductility and a large damage tolerance to ensure that the coating does not peel or crack under the impact of foreign particles and the influence of thermal cycling [17]. In addition, materials with low thermal conductivity can play a certain role in insulation, thereby reducing the surface temperature of SiC-based composite [18].

Therefore, in this study, the mechanical properties of high-melting-point rare earth silicides YSi, $Y_5Si_4$, $Y_5Si_3$, GdSi and $Gd_5Si_4$ were assessed using first-principles calculations. These materials were selected based on the phase diagrams of Y-Si and Gd-Si binary system [19,20]. The ductility of selected silicides was evaluated according to the ratio of shear modulus to bulk modulus. Subsequently, the models proposed by Clarke [21] and Slack [22] were utilized to forecast the temperature-dependent thermal conductivity and the theoretical minimum values for Y-Si and Gd-Si silicides. The findings revealed that these yttrium and gadolinium silicides exhibit promising characteristics as potential high-temperature bond layers in EBCs applications.

## 2. Computation Methods

Density functional theory (DFT) calculations were conducted using the projection augmented wave (PAW) method [23,24]. These calculations were executed with the Vienna Ab-initio Simulation Package (VASP) [25]. A plane-wave basis cutoff energy of 520 eV was utilized, and electron spin polarization was incorporated into all calculations. Subsequently, K-point sampling in the Brillouin zone was performed using the Monkhorst–Pack method. For YSi, $Y_5Si_4$, $Y_5Si_3$, GdSi and $Gd_5Si_4$, Brillouin-zone integrations were conducted on grid sizes of $8 \times 2 \times 8$, $5 \times 2 \times 5$, $5 \times 5 \times 6$, $5 \times 8 \times 7$ and $5 \times 2 \times 5$, respectively. During the structural optimization process, which included electron self-consistent calculations, a tolerance of $10^{-4}$ eV was applied. For the computation of electron statics, a tolerance of $10^{-5}$ eV was utilized. To ensure the accuracy of mechanical and thermal properties, all lattices and atoms underwent full relaxation.

The characteristic elastic constants were calculated using the Voigt–Reuss–Hill averaging scheme [26]. Utilizing the Voigt approximation [27], the upper bulk modulus ($B_V$) and shear modulus ($G_V$) were determined as follows:

$$B_V = \frac{1}{9}(C_{11} + C_{22} + C_{33}) + \frac{2}{9}(C_{12} + C_{13} + C_{23}) \quad (1)$$

$$G_V = \frac{1}{15}(C_{11} + C_{22} + C_{33} - C_{12} - C_{13} - C_{23}) + \frac{1}{5}(C_{44} + C_{55} + C_{66}) \quad (2)$$

where the $C_{ij}$ represents the second-order elastic constants. While the Reuss approximation (lower bound) of bulk modulus ($B_R$) and shear modulus ($G_R$) were determined as follows [28]:

$$B_R = \frac{1}{(S_{11} + S_{22} + S_{33}) + 2(S_{12} + S_{13} + S_{23})} \quad (3)$$

$$G_R = \frac{15}{4(S_{11} + S_{22} + S_{33}) - 4(S_{12} + S_{13} + S_{23}) + 3(S_{44} + S_{55} + S_{66})} \quad (4)$$

in which the $S_{ij}$ are the compliance constants [29]:

$$S_{11} + S_{12} = C_{33}/C, \quad S_{11} + S_{12} = 1/(C_{11} - C_{12}),$$

$$S_{13} = -C_{13}/C, \quad S_{33} = (C_{11} + C_{12})/C, \quad S_{44} = 1/C_{44}, \quad S_{66} = 1/C_{66} \quad (5)$$

where

$$C = C_{33}\left(C_{11} + C_{12} - 2C_{13}^2\right) \tag{6}$$

The average values of the bulk modulus ($B_V$, and $B_R$) and shear modulus ($G_V$ and $G_R$) were adopted as the values of the modulus [26].

$$B = \frac{1}{2}(B_V + B_R), G = \frac{1}{2}(G_V + G_R) \tag{7}$$

The average Young's modulus ($E$) and Poisson's ratio ($\mu$) were calculated using the following expression [30]:

$$E = \frac{9BG}{(3B + G)}, u = \frac{3B - 2G}{2(3B + G)} \tag{8}$$

The Vickers hardness was assessed using the following formula [31]:

$$H = 0.92\left(\frac{G}{B}\right)^{1.137} G^{0.708} \tag{9}$$

Based on $B$ and $G$ obtained from Equation (7), the mean values of the transverse ($v_T$) and longitudinal ($v_L$) sound velocity components were calculated as follows:

$$v_T = \left(\frac{G}{\rho}\right)^{\frac{1}{2}}, v_L = \left(\frac{B + \frac{4}{3}G}{\rho}\right)^{\frac{1}{2}} \tag{10}$$

where $\rho$ is the density. Then, the average velocity of sound ($v_m$) was written as [32]:

$$v_m = \left[\frac{1}{3}\left(\frac{2}{v_T^3} + \frac{1}{v_L^3}\right)\right]^{\frac{-1}{3}} \tag{11}$$

Based on this, the Debye temperature ($\Theta_D$) was obtained as [32]:

$$\Theta_D = \frac{h}{k_B}\left[\frac{3n}{4\pi}\left(\frac{N_A\rho}{M}\right)\right]^{\frac{1}{3}} v_m \tag{12}$$

where $n$ represents the number of atoms in a formula unit, $k_B$ denotes the Boltzmann constant, $h$ signifies the Planck constant, $N_A$ is the Avogadro constant, and $M$ corresponds to the molecular weight.

At lower temperature ($0.5\,\Theta_D < T < 1.6\,\Theta_D$), the thermal conductivity ($k$) was calculated from Slack's model [22]:

$$k = A\frac{\overline{M}\Theta^3\delta}{\gamma^2 n^{\frac{2}{3}} T} \tag{13}$$

where $\delta$: cube root of the average volume of the atom, $\overline{M}$: the average mass of the atoms in the crystal, $A$: a physical constant, $\gamma$: Grüneisen's parameter [33]:

$$\gamma = \frac{9\left(v_L^2 - \frac{4}{3}v_T^2\right)}{2\left(v_L^2 - 2v_T^2\right)} = \frac{3(1 + v_m)}{2(2 - 3v_m)} \tag{14}$$

Thermal conductivity decreases with increasing temperature and then saturated to a constant value ($k_{min}$), which was determined using the Clarke's model [21]:

$$k_{min} = 0.257k_B^2\hbar^{-1}\langle M\rangle^{-\frac{1}{3}}\rho^{\frac{1}{3}}\Theta_D \tag{15}$$

where <*M*> is the average atomic mass equal to $M/N_A n_a$ ($n_a$ is the number of atoms in a molecule), $\hbar$ represents the reduced Planck constant ($h/2\pi$).

## 3. Results and Discussion

### 3.1. Structural Properties

For YSi, $Y_5Si_4$, $Y_5Si_3$, GdSi, and $Gd_5Si_4$ with *Cmcm*, *Pnma*, $P6_3/mcm$, *Pnma* and *Pnma* space groups, the structural parameters were firstly optimized. Both $Y_xSi_y$ and $Gd_xSi_y$ crystals for structural optimization are single-cell, as shown in Figure 1. The calculated structural parameters and JCPDS data are listed in Table 1 (the JCPDS card of $Y_5Si_4$ was not retrieved), and it can be seen that the structural parameters calculated by first principles are consistent with the JCPDS card data.

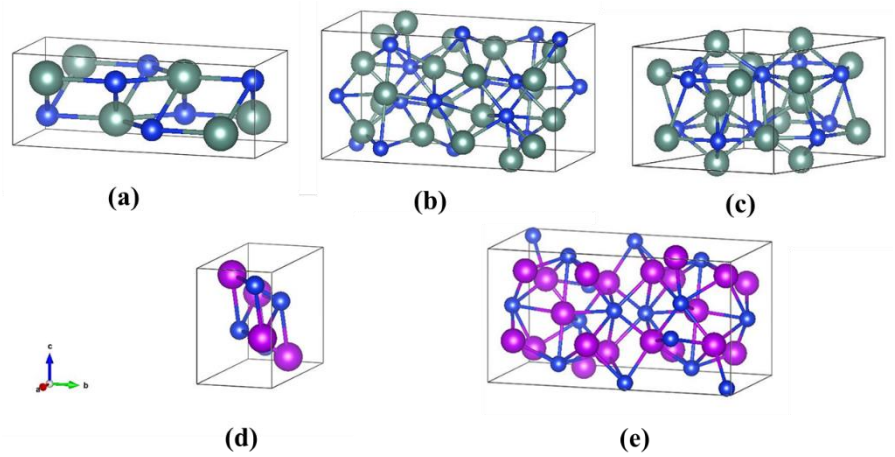


**Figure 1.** Crystal structures of $Y_xSi_y$ and $Gd_xSi_y$: (**a**) YSi, (**b**) $Y_5Si_4$, (**c**) $Y_5Si_3$, (**d**) GdSi, (**e**) $Gd_5Si_4$ (the blue-colored ball represented Si atoms, the green-colored ball represented Y atoms and the purple-colored ball represented Gd atoms).

**Table 1.** Calculated equilibrium lattice parameters of $Y_xSi_y$ and $Gd_xSi_y$ compared to their JCPDS card data.

| Materials | *a*(Å) | *b*(Å) | *c*(Å) |
|---|---|---|---|
| YSi | 4.283 | 10.541 | 3.842 |
| YSi (89-2305) | 4.251 | 10.526 | 3.826 |
| $Y_5Si_4$ | 7.443 | 14.585 | 7.701 |
| $Y_5Si_3$ | 8.445 | 8.445 | 6.386 |
| $Y_5Si_3$ (89-3037) | 8.403 | 8.403 | 6.303 |
| GdSi | 7.980 | 3.878 | 5.767 |
| GdSi (80-0705) | 7.973 | 3.858 | 5.753 |
| $Gd_5Si_4$ | 7.516 | 14.735 | 7.774 |
| $Gd_5Si_4$ (87-2319) | 7.486 | 14.750 | 7.751 |

In addition, to clearly see the accuracy of the calculation, the relative errors of lattice constants for $Y_xSi_y$ and $Gd_xSi_y$ compared to JCPDS data are plotted (Figure 2). The maximum observed relative error is 1.317% for the $Y_5Si_3$ crystal, while errors for other materials are less than 0.8%. This further illustrated the accuracy of the calculation results.

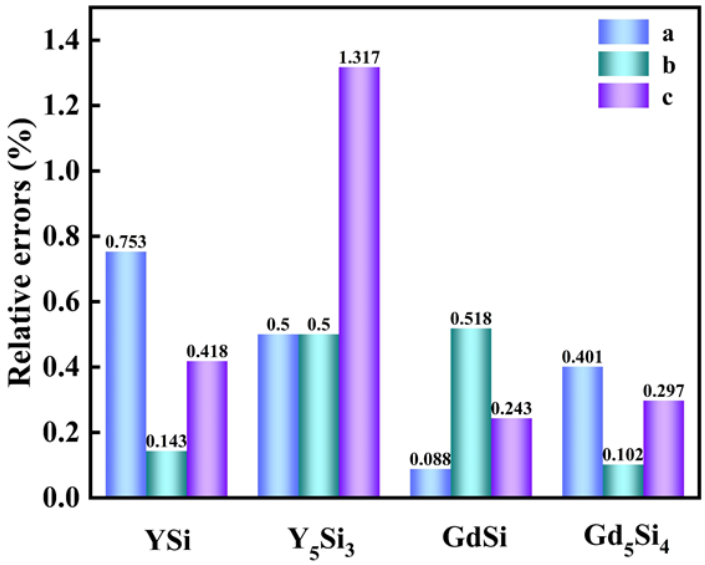


**Figure 2.** Relative errors of lattice constants of $Y_xSi_y$ and $Gd_xSi_y$.

### 3.2. Elastic and Mechanical Properties

The elastic constants, as calculated, are listed in Table 2. It can be seen that $Y_5Si_3$, which is a tetragonal structure, has six independent elastic constants; YSi, $Y_5Si_4$, GdSi and $Gd_5Si_4$ are orthomorphic structures, each have nine independent elastic constants. To evaluate the mechanical stability of $Y_xSi_y$ and $Gd_xSi_y$, Born's requirements for tetragonal structures were given as follows [34–36]:

$$(C_{11} - C_{12}) > 0,\ (C_{11} + C_{33} - 2C_{13}) > 0,\ C_{11} > 0,\ C_{33} > 0,\ C_{44} > 0, C_{66} > 0,\ (2C_{11} + C_{33} + 2C_{12} + 4C_{13}) > 0 \quad (16)$$

**Table 2.** Calculated elastic constants $C_{ij}$ (in GPa) for $Y_xSi_y$ and $Gd_xSi_y$.

| Materials | $C_{11}$ | $C_{12}$ | $C_{13}$ | $C_{22}$ | $C_{23}$ | $C_{33}$ | $C_{44}$ | $C_{55}$ | $C_{66}$ |
|---|---|---|---|---|---|---|---|---|---|
| YSi | 161 | 43 | 67 | 203 | 25 | 182 | 48 | 101 | 62 |
| $Y_5Si_4$ | 119 | 37 | 51 | 139 | 50 | 139 | 44 | 31 | 52 |
| $Y_5Si_3$ | 167 | 40 | 32 | | | 119 | 51 | | 62 |
| GdSi | 161 | 43 | 67 | 203 | 25 | 182 | 48 | 101 | 62 |
| $Gd_5Si_4$ | 107 | 36 | 48 | 134 | 50 | 130 | 38 | 31 | 51 |

And for orthorhombic crystals are [36]:

$$\begin{gathered}(C_{11} + C_{22} - 2C_{12}) > 0,\ (C_{11} + C_{33} - 2C_{13}) > 0,\ (C_{22} + C_{33} - 2C_{23}) > 0,\ C_{11} > 0,\\ C_{22} > 0, C_{33} > 0, C_{44} > 0, C_{55} > 0, C_{66} > 0, (C_{11} + C_{22} + C_{33} + 2C_{12} + 2C_{13} + 2C_{23}) > 0\end{gathered} \quad (17)$$

Based on these requirements and calculated elastic constants, these five $Y_xSi_y$ and $Gd_xSi_y$ considered in this paper were all mechanically stable.

The calculated mechanical properties of $Y_xSi_y$ and $Gd_xSi_y$ are tabulated in Table 3. *B* represents the elasticity of a substance within the elastic range, and for YSi, the *B* value is the largest among the silicides in Table 3, indicating that YSi has the strongest incompressibility. *G* describes the resistance to shape change in materials, with a lower value indicating higher ductility. For $Y_xSi_y$ and $Gd_xSi_y$, the *G* value is obviously smaller than *B*, suggesting good ductility and machinability. A lower value of *E* can reduce the impact of thermal stress and potentially extend the service life of the coating materials [37]. As shown in Table 3, in the Y-Si system, the order of the calculated *E* is YSi > $Y_5Si_3$ > $Y_5Si_4$, and in the Gd-Si system, it is GdSi > $Gd_5Si_4$. Specifically, the calculated *E* value for $Gd_5Si_4$ is only 94 GPa (Table 3), which is significantly lower than that of the traditional Si bond layer (140 ± 2 GPa) [38].

**Table 3.** Calculated bulk modulus ($B$), shear modulus ($G$), Young's modulus ($E$), Poisson's ratio ($\mu$), and hardness ($H$) of $Y_xSi_y$ and $Gd_xSi_y$.

| Materials | $B$ (GPa) | $G$ (GPa) | $E$ (GPa) | $\mu$ | $H$ (HV) | $G/B$ |
|---|---|---|---|---|---|---|
| YSi | 91 | 67 | 161 | 0.205 | 13 | 0.736 |
| $Y_5Si_4$ | 75 | 42 | 106 | 0.265 | 7 | 0.560 |
| $Y_5Si_3$ | 71 | 56 | 133 | 0.194 | 12 | 0.789 |
| GdSi | 74 | 57 | 136 | 0.193 | 12 | 0.730 |
| $Gd_5Si_4$ | 62 | 38 | 94 | 0.247 | 7 | 0.613 |

Furthermore, materials that serve as high-temperature coatings must also exhibit plasticity, as the plastic deformation process is crucial for the effective release of thermal stress. The toughness and brittleness of the material can be judged by Equation (8), if $\mu > 0.26$, the material is more plastic than brittle [39]. As shown in Table 3, Poisson's ratio of $Y_5Si_4$ was more than 0.26. This showed that $Y_5Si_4$ is relative plastic, and the rest are more brittle. In addition, the calculation is performed at zero temperature and zero pressure, in which case the hardness order of Y $Y_xSi_y$ and $Gd_xSi_y$ was YSi > $Y_5Si_3$ = GdSi > $Y_5Si_4$ = $Gd_5Si_4$. A small $G/B$ ratio indicates good ductility, processability, and damage tolerance, which helps to maintain the integrity of the coating. This property prevents issues such as foreign particle impact and thermal cycling, as well as avoiding cracks that can be caused by thermal expansion mismatches. After calculation, the order of $G/B$ values is $Y_5Si_3$ > YSi > GdSi > $Gd_5Si_4$ > $Y_5Si_4$. It is predicted that $Y_5Si_4$ has the best ductility among these materials.

Young's modulus ($E$) can be used to evaluate the strength and stiffness of a material. In practical applications, it needs to accurately obtain the 3D Young's modulus diagram to understand the change in $E$ with crystal orientation. In the case of $Y_xSi_y$ and $Gd_xSi_y$, the relation between $E$ and direction can be obtained by the following equation [40]:

$$\frac{1}{E} = l_1^4 + 2l_1^2l_2^2s_{12} + 2l_1^2l_3^2s_{13} + l_2^4s_{22} + 2l_2^2l_3^2s_{23} + l_3^4s_{33} + l_2^2l_3^2s_{44} + l_1^2l_3^2s_{55} + l_1^2l_2^2s_{66} \quad (18)$$

The elastic compliance $S_{ij}$ is related to the directional cosines $l_1$, $l_2$, and $l_3$ with respect to the three principal directions. The surface contours of $E$ for $Y_xSi_y$ and $Gd_xSi_y$ are depicted in Figure 3a–e, and the planar projections of $E$ for (100), (010), and (001) crystallographic planes are shown in Figure 3(a1–e1). According to [41], crystal directions $A$ and $B$ correspond to different crystallographic orientations on various planes: for the (001) plane, $A$ corresponds to the [100] direction and $B$ to the [010] direction; for the (010) plane, they correspond to the [100] direction and the [001] direction, respectively; and for the (100) plane, they are the [001] direction and the [010] direction.

Figure 3 clearly illustrates the elastic anisotropy of $Y_xSi_y$ and $Gd_xSi_y$. For YSi, the anisotropy of $E$ on the (001) plane was stronger than on the other two planes, with the minimum $E$ occurring in the <100> direction (Figure 3(a,a1)). For $Y_5Si_3$, the anisotropy of the (010) and (100) crystal planes are the same, and the minimum and maximum values occur in the <001> and <100> directions, respectively (Figure 3(c,c1)). For $Y_5Si_4$ (Figure 3(b,b1)), GdSi (Figure 3(d,d1)) and $Gd_5Si_4$ (Figure 3(e,e1)), the anisotropy of $E$ on the (010) plane is stronger than on the other two planes. Based on the above analysis, the degree of anisotropy of Young's modulus correlates closely with crystal symmetry. According to Mohapatra and Eckhardt [42], the anisotropy of the elastic modulus is primarily influenced by the non-diagonal elements of the compliance matrix. Therefore, if these non-diagonal elements (i.e., $S_{12}$, $S_{13}$, $S_{23}$, in this case) are ignored when calculating 3D Young's modulus, the degree of anisotropy will be significantly reduced. This explains why, among the materials mentioned, $Y_5Si_3$ exhibits the lowest degree of anisotropy in Young's modulus. The anisotropy data for the elastic properties of $Y_xSi_y$ and $Gd_xSi_y$ depicted in Figure 3 can offer substantial support for the design, selection, and simulation of materials.

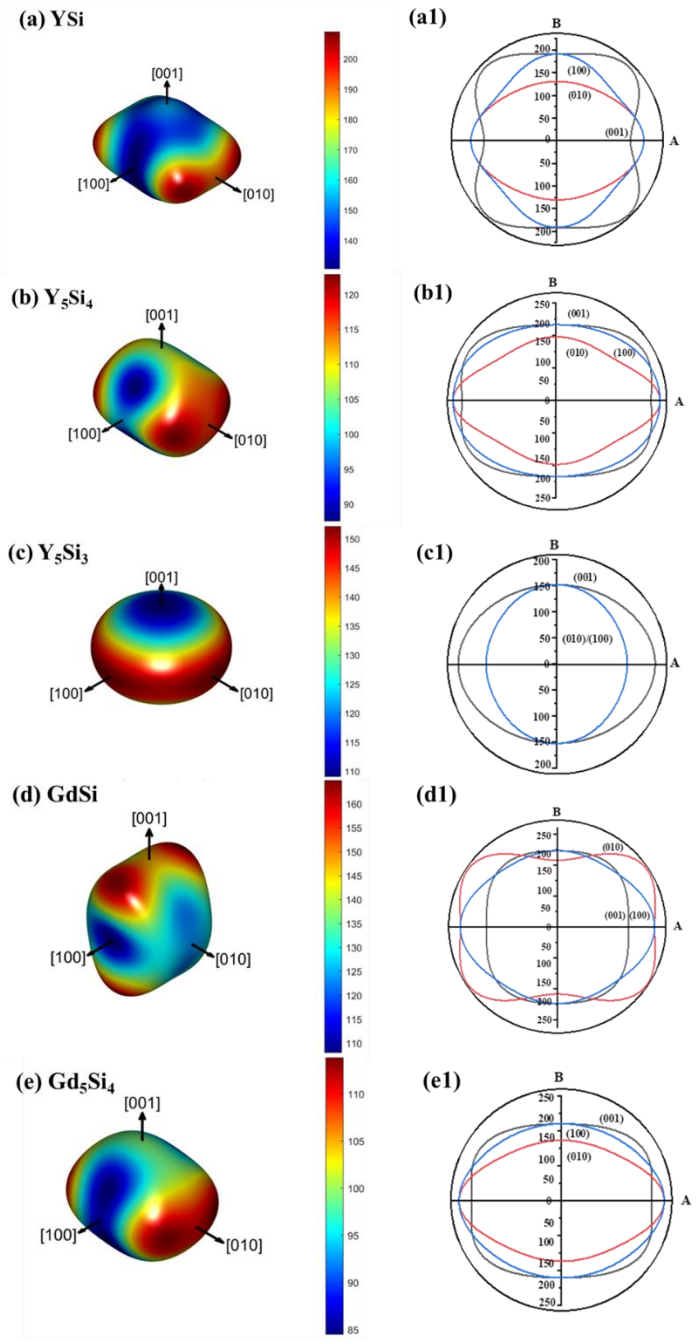


**Figure 3.** Surface contour of direction-dependent Young's modulus (**a**) YSi, (**b**) $Y_5Si_4$, (**c**) $Y_5Si_3$, (**d**) GdSi, (**e**) $Gd_5Si_4$, (**a1**–**e1**) are planar projections on (100), (010), and (001) crystallographic planes.

### *3.3. Thermal Conductivity*

Coatings with low thermal conductivity possess strong thermal insulation capabilities, effectively mitigating the thermal damage from the environment to the matrix. Therefore, thermal conductivity is a critical factor to consider when selecting suitable EBCs. According to Equations (13) and (15), the estimation of the intrinsic thermal conductivity of $Y_xSi_y$ and $Gd_xSi_y$ depends on the $v_L$, $v_T$, $v_m$, and $\Theta_D$. According to Equations (10)–(12), the calculation results for the aforementioned parameters are listed in Table 4. The results indicate that the sound velocities of $Gd_xSi_y$ are significantly lower than those of $Y_xSi_y$. Additionally, the order of $\Theta_D$ values is YSi > $Y_5Si_3$ > $Y_5Si_4$ > GdSi > $Gd_5Si_4$. Figure 4 displays a comparison between the $\Theta_D$ values calculated in this study and those from the literature. The minimal

difference between the calculated and reported values suggests that the results of our calculations are reliable.

**Table 4.** Calculated sound velocities ($v_L$, $v_T$, $v_m$), Debye temperature ($\Theta_D$), and minimum thermal conductivity ($k_{min}$) of $Y_xSi_y$ and $Gd_xSi_y$.

| Materials | $v_L$ (km/s) | $v_T$ (km/s) | $v_m$ (km/s) | $\Theta_D$·(K) | $k_{min}$(w/(m·K)) |
|---|---|---|---|---|---|
| YSi | 6.34 | 3.86 | 4.27 | 455 | 0.76 |
| $Y_5Si_4$ | 5.44 | 3.08 | 3.42 | 356 | 0.58 |
| $Y_5Si_3$ | 5.75 | 3.54 | 3.91 | 398 | 0.63 |
| GdSi | 4.65 | 2.87 | 3.17 | 335 | 0.55 |
| $Gd_5Si_4$ | 4.03 | 2.34 | 2.59 | 267 | 0.43 |

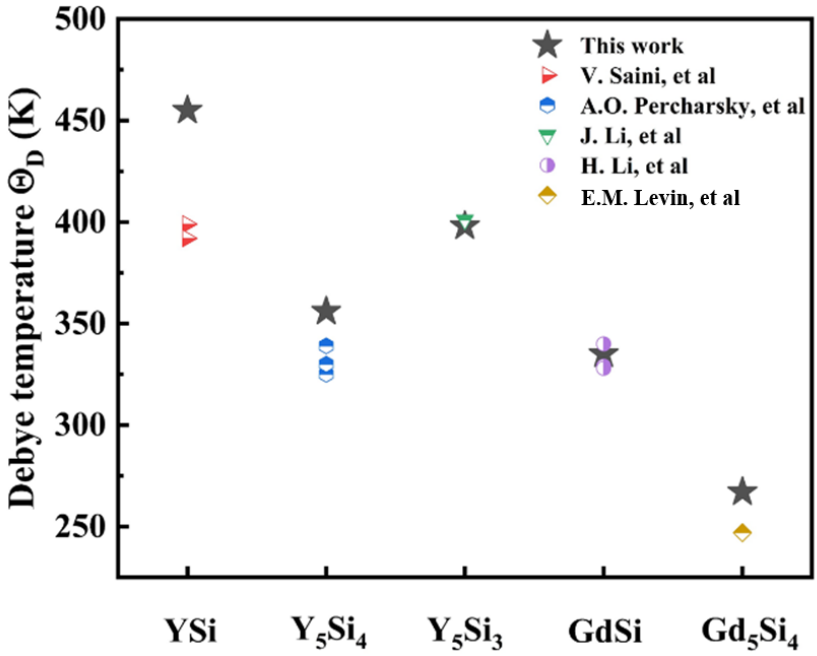


**Figure 4.** Comparison of the calculated Debye temperature of $Y_xSi_y$ and $Gd_xSi_y$ with reference values [43–47].

The material's inherent thermal conductivity is determined by how phonons interact and scatter at varying temperature levels [21]. Slack's model, as presented in Equation (13) [22], offers a suitable approach to temperature-dependent thermal conductivity at a relatively low temperature. The model-estimated temperature-dependent thermal conductivity for $Y_xSi_y$ and $Gd_xSi_y$ is in Figure 5. It can also be intuitively seen from Figure 5 that although the slopes of each curve were different, they all exhibit an inverse proportionality to temperature. Based on Slack's model, the behavior of thermal transportation $Y_xSi_y$ could be described the following: with the increase in temperature, the thermal conductivity of YSi, $Y_5Si_4$, and $Y_5Si_3$ declined as $k = 989.11/T$, $k = 902.99/T$ and $k = 531.61/T$. Similarly, the thermal conductivity of GdSi and $Gd_5Si_4$ in relation to temperature was $k = 579.48/T$ and $k = 313.53/T$, respectively. Then, if the temperature is higher, the phonon mean free path will reduce to the average atomic distances when the thermal conductivity is close to the minimum [21]. As Slack's model does not provide a rigorous theory for high-temperature thermal conductivity, this study utilized the modified Clarke's model (Equation (15)) to assess the minimum thermal conductivity ($k_{min}$). Table 4 indicates a calculated thermal conductivity sequence for $Y_xSi_y$ and $Gd_xSi_y$ as follows: $Gd_5Si_4 < Y_5Si_3 <$ GdSi $< Y_5Si_4 <$ YSi, with $Gd_5Si_4$ exhibiting the lowest thermal conductivity at 0.43 W $m^{-1}$ $K^{-1}$. Calculations revealed that the thermal conductivities of $Gd_xSi_y$ compounds are lower than that of silicides in the Y-Si system, suggesting that when used as coating materials, specific compounds such

as GdSi and $Gd_5Si_4$ will exhibit superior thermal insulation ability, potentially mitigating thermal damage to the SiC composites substrate.

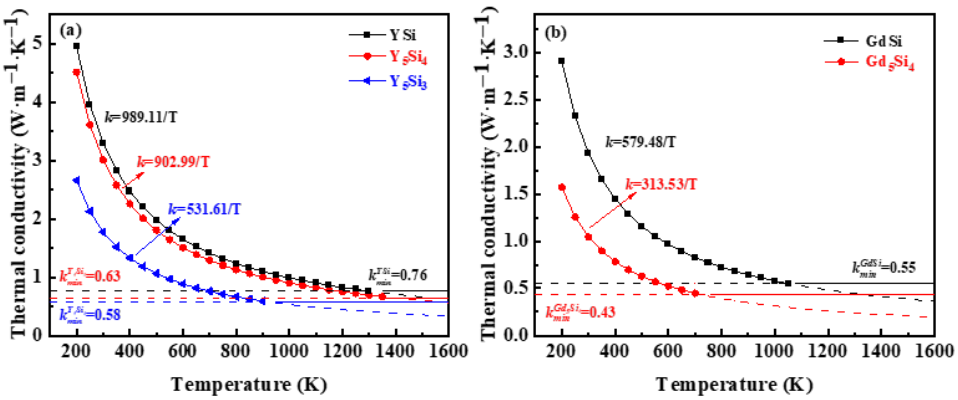


**Figure 5.** Relationship of thermal conductivity with temperature for (**a**) $Y_xSi_y$ and (**b**) $Gd_xSi_y$. Solid line represents the minimum value of thermal conductivity.

## 4. Conclusions

In this work, the elastic constants of silicides YSi, $Y_5Si_4$, $Y_5Si_3$, GdSi, and $Gd_5Si_4$ in the Y-Si and Gd-Si systems were predicted using first-principles calculations. Subsequently, the volume modulus, shear modulus, Young's modulus, sound velocity, Debye temperature, and thermal conductivity were calculated by empirical formulas. The optimized structural parameters of $Y_xSi_y$ and $Gd_xSi_y$ showed minimal differences compared to the existing JCPDS card data. The conclusions regarding their mechanical and thermal properties are as follows:

(1) The results for elastic properties indicated that $Y_5Si_4$ is a ductile material, and its $G/B$ value is lower than that of the other materials in this study. This characteristic helps to minimize the thermal stress and enhances the thermal shock resistance when used as coating materials. In addition, Young's moduli of all the calculated materials are anisotropic.

(2) The calculated thermal conductivity sequence for $Y_xSi_y$ and $Gd_xSi_y$ is as follows: $Gd_5Si_4$ < $Y_5Si_3$ < GdSi < $Y_5Si_4$ < YSi, with $Gd_5Si_4$ exhibiting the lowest thermal conductivity at 0.43 W $m^{-1}$ $K^{-1}$. This study ascertains that they are promising materials for environmental barrier coatings.

**Author Contributions:** K.P.: writing—review and editing; software; investigation; methodology. P.H.: writing—original draft; Formal analysis; Investigation; methodology. G.H.: supervision; writing—review and editing; resources; funding acquisition. H.L.: software; methodology. W.Z., W.W. and J.Z.: resources; supervision. All authors have read and agreed to the published version of the manuscript.

**Funding:** This work was supported by the National Natural Science Foundation of China (No. 51902183).

**Data Availability Statement:** Data will be made available on reasonable request.

**Conflicts of Interest:** The authors declare no known competing financial interests.

## References

1. Przyborowski, M.; Hibiya, T.; Eguchi, M.; Egry, I. Surface tension measurement of molten silicon by the oscillating drop method using electromagnetic levitation. *J. Cryst. Growth* **1995**, *151*, 60–65. [CrossRef]
2. Sullivan, R.M. Reformulation of oxide growth equations for oxidation of silicon bond coat in environmental barrier coating systems. *J. Eur. Ceram. Soc.* **2019**, *39*, 5403–5409. [CrossRef]
3. Damby, D.E.; Llewellin, E.W.; Horwell, C.J.; Williamson, B.J.; Najorka, J.; Cressey, G.; Carpenter, M. The α–β phase transition in volcanic cristobalite. *J. Appl. Crystallogr.* **2014**, *47*, 1205–1215. [CrossRef] [PubMed]

4. Zhang, Z.; Park, Y.; Xue, Z.; Zhang, S.; Byon, E.; Koo, B. Research status of bond coats in environmental barrier coatings. *Int. J. Appl. Ceram. Technol.* **2022**, *19*, 1841–1859. [CrossRef]
5. Tejero-Martin, D.; Bennett, C.; Hussain, T. A review on environmental barrier coatings: History, current state of the art and future developments. *J. Eur. Ceram. Soc.* **2021**, *41*, 1747–1768. [CrossRef]
6. Deijkers, J.A.; Wadley, H.N.G. Hafnium silicate formation during oxidation of a permeable silicon + $HfO_2$ powder composite system. *Acta Mater.* **2020**, *201*, 448–461. [CrossRef]
7. Suzuki, A.; Ashida, H.; Furui, N.; Mameno, K.; Matsunami, H. Thermal Oxidation of SiC and Electrical Properties of Al-$SiO_2$-SiC MOS Structure. *Jpn. J. Appl. Phys.* **1982**, *36*, 3770–3778. [CrossRef]
8. Anton, R.; Leisner, V.; Watermeyer, P.; Engstler, M.; Schulz, U. Hafnia-doped silicon bond coats manufactured by PVD for SiC/SiC CMCs. *Acta Mater.* **2020**, *183*, 471–483. [CrossRef]
9. Xiao, S.; Li, J.; Liu, X.; Chang, Z.; Huang, P.; Zhang, A.; Tian, Y.; Zhang, X.; Zhang, J.; Han, G. Exploration of the oxidation behavior and doping ratio of the Si–$HfO_2$ bond layer used in environmental barrier coatings. *Int. J. Appl. Ceram. Technol.* **2023**, *20*, 1753–1763. [CrossRef]
10. Chen, W.; Han, Q.; He, J.; He, W.; Wang, W.; Guo, H. Effect of $HfO_2$ framework on steam oxidation behavior of $HfO_2$ doped Si coating at high temperatures. *Ceram. Int.* **2022**, *48*, 22209–22210. [CrossRef]
11. Sun, Z.; Li, M.; Zhou, Y. Thermal properties of single-phase $Y_2SiO_5$. *J. Eur. Ceram. Soc.* **2009**, *29*, 551–557. [CrossRef]
12. Ogura, Y.; Kondo, M.; Morimoto, T.; Notomi, A.; Sekigawa, T. Oxygen permeability of $Y_2SiO_5$. *Mater. Trans.* **2001**, *42*, 1124–1130. [CrossRef]
13. Tian, Z.; Zhang, J.; Zhang, T.; Ren, X.; Hu, W.; Zheng, L.; Wang, J. Towards thermal barrier coating application for rare earth silicates $RE_2SiO_5$ (RE= La, Nd, Sm, Eu, and Gd). *J. Eur. Ceram. Soc.* **2019**, *39*, 1463–1476. [CrossRef]
14. Dong, Y.; Ren, K.; Wang, Q.; Shao, G.; Wang, Y. Interaction of multicomponent disilicate $(Yb_{0.2}Y_{0.2}Lu_{0.2}Sc_{0.2}Gd_{0.2})_2Si_2O_7$ with molten calcia-magnesia-aluminosilicate. *J. Adv. Ceram.* **2022**, *11*, 66–74. [CrossRef]
15. Ramasamy, S.; Tewari, S.N.; Lee, K.N.; Bhatt, R.T.; Fox, D.S. Environmental durability of slurry based mullite–gadolinium silicate EBCs on silicon carbide. *J. Eur. Ceram. Soc.* **2011**, *31*, 1123–1130. [CrossRef]
16. Kim, S.-H.; Kim, B.-N.; Nagashima, N.; Matsushita, Y.; Jang, B.-K. High-temperature corrosion of spark plasma sintered Gd2SiO5 with volcanic ash for environmental barrier coatings. *J. Eur. Ceram. Soc.* **2021**, *41*, 3161–3166. [CrossRef]
17. Lee, K.N.; Eldridge, J.I.; Robinson, R.C. Residual stresses and their effects on the durability of environmental barrier coatings for SiC ceramics. *J. Am. Ceram. Soc.* **2005**, *88*, 3483–3488. [CrossRef]
18. Olson, D.H.; Deijkers, J.A.; Quiambao-Tomko, K.; Gaskins, J.T.; Richards, B.T.; Opila, E.J.; Hopkins, P.E.; Wadley, H.N. Evolution of microstructure and thermal conductivity of multifunctional environmental barrier coating systems. *Mater. Today Phys.* **2021**, *17*, 100304. [CrossRef]
19. Shukla, A.; Kang, Y.B.; Pelton, A.D. Thermodynamic assessment of the Ce–Si, Y–Si, Mg–Ce–Si and Mg–Y–Si systems. *Int. J. Mater. Res.* **2009**, *100*, 208–217. [CrossRef]
20. Huang, M.; Schlagel, D.L.; Schmidt, F.A.; Lograsso, T.A. Experimental Investigation and Thermodynamic Modeling of the Gd—Si System. *J. Alloys Compd.* **2007**, *441*, 94–100. [CrossRef]
21. Clarke, D.R. Materials selection guidelines for low thermal conductivity thermal barrier coatings. *Surf. Coat. Technol.* **2003**, *163*, 67–74. [CrossRef]
22. Slack, G.A. Nonmetallic crystals with high thermal conductivity. *J. Phys. Chem. Solids* **1973**, *34*, 321–335. [CrossRef]
23. Kresse, G.; Joubert, D. From ultrasoft pseudopotentials to the projector augmented-wave method. *Phys. Rev. B* **1999**, *59*, 1758–1775. [CrossRef]
24. Blöchl, P.E. Projector augmented-wave method. *Phys. Rev. B* **1994**, *50*, 17953–17979. [CrossRef] [PubMed]
25. Kresse, G.; Furthmüller, J. Efficient Iterative Schemes for Ab Initio Total-Energy Calculations Using a Plane-Wave Basis Set. *Phys. Rev. B Condens. Matter* **1996**, *54*, 11169–11186. [CrossRef] [PubMed]
26. Hill, R. The elastic behavior of crystalline aggregate. *Proc. Phys. Society. Sect. A* **1952**, *65*, 349–354. [CrossRef]
27. Voigt, W. *Lehrbuch der Kristallphysik*; Teubner: Leipzig, Germany, 1928.
28. Reuss, A. Calculation of the flow limits of mixed crystals on the basis of the plasticity of monocrystals. *Z. Angew. Math. Mech.* **1929**, *9*, 49–58. [CrossRef]
29. Nye, J.F. *Physical Properties of Crystals: Their Representation by Tensors and Matrices*; Oxford University Press: Oxford, UK, 1985.
30. Green, D.J. *An Introduction to the Mechanical Properties of Ceramics*; Cambridge University Press: Cambridge, UK, 1998; pp. 1–12.
31. Nazipov, D.V. First-Principles Study of Elastic Properties of Rare-Earth Oxyorthosilicates $R_2SiO_5$. *Phys. Status Solidi (B)* **2021**, *258*, 2100181. [CrossRef]
32. Anderson, O.L. A simplified method for calculating the debye temperature from elastic constants. *J. Phys. Chem. Solids* **1963**, *24*, 909–917. [CrossRef]
33. Sanditov, B.D.; Tsydypov, S.B.; Sanditov, D.S. Relation between the Grüneisen constant and Poisson's ratio of vitreous systems. *Acoust. Phys.* **2007**, *53*, 594–597. [CrossRef]
34. Beckstein, O.; Klepeis, J.E.; Hart, G.L.; Pankratov, O. First-principles elastic constants and electronic structure of α-$Pt_2Si$ and PtSi. *Phys. Rev. B* **2001**, *13*, 134112. [CrossRef]
35. Wu, Z.J.; Zhao, E.J.; Xiang, H.P.; Hao, X.F.; Liu, X.J.; Meng, J. Publisher's Note: Crystal structures and elastic properties of superhard $IrN_2$ and $IrN_3$ from first principles [Phys. Rev. B 76, 054115 (2007)]. *Phys. Rev. B* **2007**, *76*, 059904. [CrossRef]

36. Schfer, K. Duane C. Wallace: Thermodynamics of Crystals. In *Berichte der Bunsengesellschaft für Physikalische Chemie*; Verlag Chemie: Weinheim, Germany, 1972; Volume 76.
37. Makishima, A.; Mackenzie, J.D. Calculation of bulk modulus, shear modulus and Poisson's ratio of glass. *J. Non-Cryst. Solids* **1975**, *17*, 147–157. [CrossRef]
38. Kulikovsky, V.; Vorlíček, V.; Boháč, P.; Stranyánek, M.; Čtvrtlík, R.; Kurdyumov, A.; Jastrabik, L. Hardness and elastic modulus of amorphous and nanocrystalline SiC and Si films. *Surf. Coat. Technol.* **2008**, *202*, 1738–1745. [CrossRef]
39. Mattesini, M.; Magnuson, M.; Tasnádi, F.; Höglund, C.; Abrikosov, I.A.; Hultman, L. Elastic properties and electrostructural correlations in ternary scandium-based cubic inverse perovskites: A first-principles study. *Phys. Rev. B Condens. Matter* **2009**, *79*, 125122. [CrossRef]
40. Robertson, J.H. Physical properties of crystals: Their representation by tensors and matrices by J. F. Nye. *Acta Crystallogr.* **1985**, *41*, 624. [CrossRef]
41. Brantley, W.A. Calculated Elastic Constants for Stress Problems Associated with Semiconductor Devices. *J. Appl. Phys.* **1973**, *44*, 534–535. [CrossRef]
42. Mohapatra, H.; Eckhardt, C.J. Elastic constants and related mechanical properties of the monoclinic polymorph of the carbamazepine molecular crystal. *J. Phys. Chem. B* **2008**, *112*, 2293–2298. [CrossRef] [PubMed]
43. Pecharsky, A.O.; Pecharsky, V.K.; Gschneidner, K.A. Phase relationships and low temperature heat capacities of alloys in the $Y_5Si_4$–$Y_5Ge_4$ pseudo binary system. *J. Alloys Compd.* **2004**, *379*, 127–134. [CrossRef]
44. Li, J.; Zhang, X.; Fang, Z.; Cao, X.; Li, Y.; Sun, C.; Chen, Z.; Yin, F. First-principles calculations to investigate electronic, elastic, and optical properties of one dimensional electride $Y_5Si_3$. *Results Phys.* **2021**, *28*, 104615. [CrossRef]
45. Levin, E.M.; Pecharsky, V.K.; Gschneidner, K.A., Jr.; Miller, G.J. Electrical resistivity, electronic heat capacity, and electronic structure of $Gd_5Ge_4$. *Phys. Rev. B* **2001**, *64*, 235103. [CrossRef]
46. Li, H.; Xiao, Y.; Schmitz, B.; Persson, J.; Schmidt, W.; Meuffels, P.; Roth, G.; Brückel, T. Possible magnetic-polaron-switched positive and negative magnetoresistance in the GdSi single crystals. *Sci. Rep.* **2012**, *2*, 750. [CrossRef] [PubMed]
47. Saini, V.; Sasmal, S.; Kulkarni, R.; Thamizhavel, A. Linear unsaturated magnetoresistance in YSi single crystal. *Appl. Phys. Lett.* **2021**, *119*, 017904. [CrossRef]